

Bulk minority carrier lifetimes and doping of silicon bricks from photoluminescence intensity ratios

Bernhard Mitchell,^{1,a)} Thorsten Trupke,^{1,2} Jürgen W. Weber,² and Jørgen Nyhus³

¹*School of Photovoltaic and Renewable Energy Engineering, University of New South Wales, Sydney, NSW 2052, Australia*

²*BT Imaging, Surry Hills, NSW 2010, Australia*

³*REC Wafer, Norway AS, 3908 Porsgrunn, Norway*

(Received 16 February 2011; accepted 14 March 2011; published online 21 April 2011)

Two methods for spatially resolved measurement of the bulk minority carrier lifetime on the side faces of block cast silicon bricks, both based on photoluminescence imaging, are presented. The first method uses a single photoluminescence image which is normalized for variations in the background doping density. The second method is based on the measurement of the ratio of two photoluminescence images taken with different spectral filters in front of the CCD camera. This second method is advantageous over the first method since it is not dependent on an absolute measurement of the luminescence intensity and does not require a separate resistivity measurement. It is further demonstrated, that the measurement of an intensity ratio image and comparison of the latter with an individual luminescence image also allow obtaining the doping density gradient within silicon bricks. This paper presents an in-depth analysis of the underlying models, demonstrates experimental results and discusses the calibration and uncertainties of the techniques. Practical limitations and dependencies on various experimental parameters are discussed. © 2011 American Institute of Physics. [doi:10.1063/1.3575171]

I. INTRODUCTION

Knowledge of the spatially resolved bulk minority carrier lifetime within the absorber material of solar cells is of high value since it represents an important electronic material parameter, which strongly affects both the maximum voltage and the current of a solar cell. The measurement of photoluminescence images on silicon brick side faces after directional solidification can give direct feedback on the crystallization process and on feedstock quality with regard to bulk lifetime, doping, grain structures and dislocation clusters.

The determination of *bulk* lifetime is preferable over measurements of the *effective* lifetime as the latter is strongly limited by surface recombination, particularly in unpassivated samples. Silicon bricks are well suited samples for bulk lifetime measurement due to the fact that the influence of the rear surface recombination on the excess carrier profile is insignificant, resulting in much stronger variations in effective lifetime with bulk lifetime than for silicon wafers, as discussed in more detail below.

Photoluminescence (PL) imaging is a fast, spatially resolved and sensitive technique capable of detecting effective lifetime variations on silicon wafers and solar cells.¹ Würfel *et al.* presented both the theory and experimental results on using the spectral dependence of the luminescence signal on the bulk lifetime in order to extract diffusion length information from finished silicon solar cells.² The bulk lifetime information in the luminescence signal is fundamentally based on the wavelength dependent process of luminescence

photon reabsorption within the sample.³ Further studies by Giesecke *et al.* adapted the idea for the use of photo-instead of electroluminescence images applied on silicon wafer.⁴⁻⁶ However, the proximity of the rear surface in typically 180 μm thin wafers restricts the range of bulk lifetime values that can reliably be analyzed in that method to values equivalent to diffusion lengths which are in the order of the thickness of the wafer. This leads the bulk lifetime signal to only be clearly extractable for bulk lifetime values below 25 μs .^{2,4} As this limitation is fundamental it also applies for other lifetime techniques like quasi-steady-state photoconductance⁷ (QSSPC) as shown in Bothe *et al.*⁸

Bulk lifetime analysis of photoluminescence images taken on silicon bricks prior to wafer sawing has been demonstrated recently.^{9,10} This work will present the methodologies in more detail and show further experimental results as well as discussing the limitations of the approach. It will also introduce the use of the spectral dependence of the luminescence signal in order to image relative variations in the doping concentrations from the bottom to the top of the brick. With a special focus on the modeling of the spectral dependence of the luminescence, this work presents the underlying physical models leading to the luminescence intensity ratio technique.

Importantly, the calculations in this paper show that the surface recombination, which causes a strong limitation on the ability to obtain bulk information from lifetime measurements on nonpassivated silicon wafers, does not apply for nonpassivated silicon bricks. The intensity ratio transfer function is a nonsaturating function of bulk lifetime allowing a clear correlation with bulk lifetime throughout a wide range of lifetimes from 1 μs to 10 ms, thus covering the range of bulk lifetimes typical for both monocrystalline and

^{a)}Author to whom correspondence should be addressed. Electronic mail: bernhard.mitchell@student.unsw.edu.au.

multicrystalline silicon used, e.g., in photovoltaic applications.

II. THEORY

A. Bulk lifetime from a single photoluminescence image

The rate of spontaneous emission r_{sp} inside the sample determines the emitted luminescence intensity, which is proportional to the product of the carrier densities in the valence and conduction band ($r_{sp} \propto n_e n_p$). This radiative emission rate is also proportional to the average excess carrier density Δn , if so-called low injection conditions are met, i.e., if $\Delta n \ll N$ is satisfied, where N is the density of ionized dopants. The calculations discussed below show that this condition is met in typical PL imaging experiments on unpassivated silicon bricks, and it is therefore assumed in the following that:

$$r_{sp} \propto \Delta n N \quad (1)$$

Variations in the background doping density therefore need to be corrected for in an analysis of photoluminescence intensity in terms of effective or bulk lifetime. The theoretical analysis first leads to a spatially resolved transfer function $\Phi_{norm}(x, y, \tau_b)$ that describes the dependence of the background doping normalized photoluminescence intensity on the bulk lifetime.

The measured spatially resolved photoluminescence intensity $\Phi(x, y)$ is then given as

$$\Phi(x, y) = C_{cal} N(y) \Phi_{norm}(x, y, \tau_b) \quad (2)$$

where $N(y)$ is the variation in doping concentration across the ingot and it is assumed that the only significant variation in the background doping density occurs in the growth direction (y) of the ingot.

The calibration constant C_{cal} is introduced in order to allow the interpretation of uncalibrated photoluminescence intensity images $\Phi(x, y)$. The specific constant for the experimental setup used in this study is determined, by correlating the bulk lifetime data obtained from photoluminescence images with quasisteady state photoconductance (QSSPC) bulk lifetime data as described below.⁷

This correlation is not trivial due to the fact that both effective and bulk lifetime data depend on the injection level $\tau(\Delta n)$. Under steady state conditions, the effective lifetime τ_{eff} is determined by the average injection level Δn and by the average generation rate G

$$\Delta n = G \tau_{eff}(\Delta n) \quad (3)$$

As this relationship suggests, spatially resolved (quasi) steady state lifetime data can be reported either

- (a) for constant illumination intensity, which is equivalent to a constant generation rate G and results in different injection levels for each lifetime value,
- (b) for constant injection level generated by a different generation rate G for each lifetime value.

Photoluminescence images on wafer are taken with constant illumination intensity, whereas the QSSPC technique measures injection level dependent data, which is usually reported for a constant average injection level.

The following explanation will show that a single photoluminescence image allows measuring the bulk lifetime at constant illumination and also at constant and well defined average injection level, which appears to be contradictory at first sight. It is necessary in this context to consider the definition of an average carrier density and generation rate in silicon bricks. It is not meaningful to assume mean values across the sample thickness as it is typically done with thin silicon wafers. Bowden and Sinton¹¹ described that for an infinitely thick silicon brick with infinite front surface recombination velocity the continuity equation can be solved analytically for monochromatic illumination, leading to the following expression for the depth dependent excess carrier density $\Delta n(x, L)$:

$$\Delta n(x, L) = \frac{\alpha N_s L^2}{(\alpha^2 L^2 - 1)} (e^{-x/L} - e^{-\alpha x}) \quad (4)$$

with α denoting the temperature and wavelength dependent absorption coefficient of silicon, N_s the incident photon flux, and L and D the temperature and doping dependent bulk minority carrier diffusion length and diffusion constant. Figure 1 shows the excess carrier density in a silicon brick as a function of depth and bulk lifetime, revealing a strongly inhomogeneous minority carrier profile with significant excess carrier density only close to surface of the silicon brick. It is noted that only the first 0.15 cm are shown here, whereas the thickness of a silicon brick is typically 15.6 cm. The average over the sample thickness is thus not a meaningful parameter for brick in contrast to wafer measurements.

In order to overcome the problem of the nonuniformity in excess carrier density Bowden and Sinton¹¹ describe an analytical analysis methodology by defining a weighted average carrier density Δn_{avg} and an effective sample width W_{eff} , which is used in the following:

$$\Delta n_{avg} = \frac{\alpha N_s L^2}{2D(\alpha L + 1)^2} \quad (5)$$

$$W_{eff} = 2 \left(L + \frac{1}{\alpha} \right) \quad (6)$$

Assuming short wavelength illumination ($\lambda_{exc} < 800$ nm) the main variation in Δn_{avg} and W_{eff} with increasing bulk lifetime is in the effective width, while the average carrier density is almost constant. However, for longer wavelength illumination also the average injection level scales increasingly strongly with the bulk lifetime (see Fig. 1). For example in the case of an excitation wavelength of 900 nm strong variations in bulk lifetime by a factor of 10 correspond to a relative variation in average injection level of 27%, whereas an illumination below 800 nm will keep this variation below 10%.

Photoluminescence images can be performed with spatially homogeneous illumination in the 800 nm ($\alpha \approx 850 \text{ cm}^{-1}$)

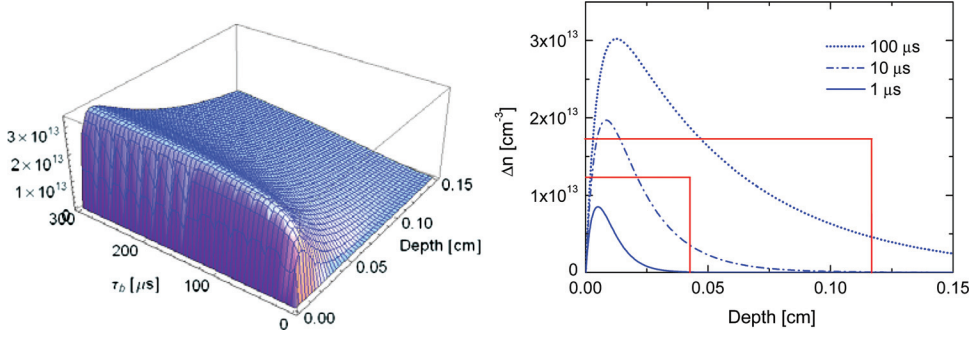


FIG. 1. (Color online) Excess carrier density $\Delta n(x, \tau_b)$ in a silicon brick as a function of bulk lifetime τ_b and absorption depth corresponding to an illumination at 900 nm and infinite surface recombination velocity after Bowden *et al.*¹¹ $\Delta n(x, \tau_b)$ globally increases with increasing bulk lifetime and the maximum of $\Delta n(x, \tau_b)$ shifts to larger sample depths. The boxes represent the values for Δn_{avg} and W_{eff} assuming a bulk lifetime of 10 and 100 μs , respectively.

range. This fulfils the condition $\alpha L \gg 1$ for $L \geq 120 \mu m$ well, and the average injection level can be assumed to be independent of the lifetime as Eq. (5) simplifies to

$$\Delta n_{avg} = \frac{N_s}{2D\alpha} \quad (7)$$

A diffusion length of $L \geq 120 \mu m$ corresponds to $\tau_b \geq 5 \mu s$ in 1 Ωcm p-type silicon at 300 K. As a result, a single photoluminescence image taken with laterally constant illumination at $\lambda_{exc} = 800 nm$ thus reports variable bulk lifetime at almost constant average injection level for $\tau_b \geq 5 \mu s$. Furthermore, the incident photon flux can be chosen in order to generate any desired average injection level and specifically allows measurement of the bulk lifetime close to the average injection level present in a finished solar cell. For industrial multicrystalline solar cells the injection level at the maximum power point is around $1 \times 10^{13} cm^{-3}$, i.e., close to the injection level that is achieved with a one-sun equivalent illumination intensity at 800 nm, as it is commonly used in PL imaging experiments.

B. Bulk lifetime and doping from a ratio of two photoluminescence images

An improved one-dimensional theoretical model has been developed in order to quantify the dependence of the photoluminescence emission spectrum and the photoluminescence intensity ratio on the bulk minority carrier lifetime in silicon bricks. The model will be discussed in detail here including the minority carrier distribution, the photon emission and detection of photons and temperature and doping dependent effects.

1. Carrier distribution

As discussed, the excess carrier distribution profile $\Delta n(x, \tau)$ within a silicon brick with infinite front surface recombination velocity and infinite thickness illuminated with monochromatic light was derived by Bowden and Sinton and is shown in Eq. (4) and Fig. 1. Considering $L = \sqrt{D\tau}$, the excess carrier concentration is a direct function of sample depth x and local bulk lifetime τ , but also an indirect function of temperature T , excitation wavelength λ and doping density, which affect the silicon absorption coefficient and mobility. This work accounts for all of these

dependencies allowing detailed predictions and analysis of parameter dependencies. The temperature dependent absorption coefficient of crystalline silicon $\alpha(T)$ was modeled according to Green¹² assuming

$$\alpha(T) = \alpha(T_0) \left(\frac{T}{T_0} \right)^{C_p(T_0)T_0} \quad (8)$$

with $T_0 = 300 K$, C_p denoting the temperature coefficient and $\alpha(T_0)$ the absorption coefficient at 300 K both listed in Green.¹² The modeling of the doping and temperature dependent minority carrier mobility of p- and n-type crystalline silicon was performed with reference to Masetti¹³ and Reggiani.¹⁴

A 5 μm thick electronically dead layer is further assumed to be present to account for the residual surface damage after a mechanical polish of the bricks. This layer will reduce excess carrier density in the underlying nondamaged silicon by about 11%, caused by the optical absorption in this layer, but does not change the relative shape of the relative carrier distribution in the case of the apparent monochromatic illumination.

In order to perform bulk lifetime measurements, the influence of the surface has to be minimized. This can be achieved by choosing longer wavelength light above 900 nm, shifting the generation profile further away from the surface.

2. Photon emission

Luminescence photons are generated by spontaneous radiative recombination of electron and holes. As the photoluminescence intensity ratio (PLIR) technique calculates the ratio of luminescence emission in certain wavelength bands, it is only necessary to account for all wavelength dependencies of the emission spectrum. There is no need to account for an absolute value due to the cancellation of nonwavelength dependent prefactors in luminescence intensity ratios. The spontaneous emission r_{sp} is therefore described as follows^{15,16}:

$$r_{sp}(\lambda, T) \propto \frac{\alpha(\lambda, T)}{\lambda^4} \exp\left(\frac{-e\hbar\omega}{kT}\right) \quad (9)$$

with $\alpha(\lambda, T)$ the silicon absorption coefficient, $\hbar\omega$ the photon energy, and T the sample temperature.

It is noted that the description of the rate of spontaneous emission as written in Eq. (9) represents the photon flux per constant wavelength interval. The expression for the absolute rate of spontaneous emission contains the wavelength dependent refractive index but is not accounted for in Eq. (9) due to the fact that it is almost constant between 900 and 1200 nm.^{12,17}

3. Detection of emitted photons

A monochromatic light source is used to excite excess carriers within the brick which then emits a temperature dependent band-to-band luminescence spectrum in the bulk of the brick. The fundamental process of photon reabsorption of luminescence radiation within the sample changes the luminescence spectrum on its optical path through the sample toward the detection device. This generates a spectral dependency which causes the spectrum to contain information about the relative excess carrier density profile and thereby about bulk lifetime. The spectral dependence of the photon reabsorption is caused by the spectral dependence of the absorption coefficient, which shows its most pronounced variation around the bandedge, i.e., exactly in the spectral region where the silicon luminescence occurs. In result short wavelength luminescence will only be able to contribute to the signal if emitted very close to the surface, whereas long wavelength luminescence has a much lower probability of being reabsorbed. For example the crystalline silicon absorption coefficient takes on values exceeding 65 cm^{-1} for wavelengths below 1000 nm and is below 22 cm^{-1} for wavelengths above 1050 nm resulting in a ratio of greater than three.

The large thickness of the silicon bricks simplifies the analysis of the spectral dependency in comparison to a silicon wafer, where the optical and electronic properties of the rear surface significantly affect the carrier profile. These factors significantly complicate the analysis for thin wafers and cells and lead to large uncertainties and inaccuracies.⁴ For thick silicon bricks none of these uncertainties exist.

Figure 2 illustrates calculated spontaneous emission spectra with and without reabsorption on a $500 \mu\text{m}$ optical path for two different temperatures corresponding to Eq. (9) extended by a reabsorption term.

In the two-filter method two spectral edge pass filters are used in order to detect signals in two different spectral regions: A first PL signal is measured with a short pass filter representing the carrier density near the front surface. A second signal is measured with a long pass filter, representing the carrier density deeper inside the brick. Figure 3 shows the resulting detected luminescence signal as a function of wavelength and bulk lifetime after integration over the depth profile. All spectral dependencies of the optical setup are considered in the calculation including the CCD quantum efficiency. Both spectra filtered by short and long pass are shown in Fig. 3 for increasing bulk lifetimes. It can be seen that the long pass spectrum shows a stronger increase with bulk lifetime due to the fact that the main variation in excess carrier density with increasing bulk lifetime occurs deep inside the brick (compare Fig. 1). The shift of the spectra

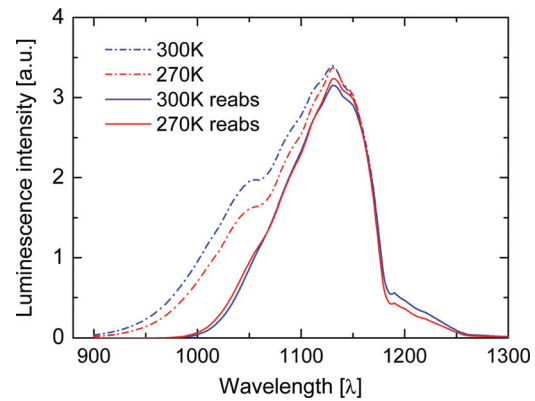


FIG. 2. (Color online) Luminescence intensity spectrum emitted by a volume element at a depth of $500 \mu\text{m}$ with and without photon reabsorption calculated for 270 and 300 K sample temperature. A strongly reduced signal in the short wavelength range of the spectrum is visible. The temperature dependence of the spectrum is reduced in case of a long optical pathway as it is chosen here.

toward shorter wavelength in comparison to the total emission spectrum shown in Fig. 2 is mainly due to the low silicon CCD sensitivity above 1000 nm.

Numerical integration of the luminescence signal through the entire depth of the brick and across the respective wavelength range according to Eq. (10) gives the measured luminescence signal as a function of the bulk lifetime:

$$PL(\tau_b) = \int_0^d \int_{\lambda_0}^{\lambda} r_{sp}(\lambda) \Delta n(x, \tau_b) e^{-\alpha(\lambda)x} \Theta(\lambda) d\lambda dx \quad (10)$$

where the exponential term accounts for the photon reabsorption and $\theta(\lambda)$ represents the spectral characteristics of the optical system including filters, objective and CCD camera. Equation (10) describes the rate of spontaneous emission to be proportional to the excess carrier density, i.e., it assumes low injection conditions, which is a good assumption for most practical scenarios due to the low excess carrier densities that are achieved in PL imaging on bricks (compare Fig. 1). Modifications to account for medium to high injection would be required only for very high resistivity material ($>100 \Omega\text{cm}$).

The photoluminescence intensity ratio is defined as a function of bulk lifetime correspondingly:

$$PLIR(\tau_b) = \frac{PL_{longpass}(\tau_b)}{PL_{shortpass}(\tau_b)} \quad (11)$$

This measure purely relies on the knowledge of all relative spectral dependencies in the experimental setup and does not rely on the absolute knowledge of parameters such as laser power and sample reflectivity. Most importantly, the ratio eliminates variations in the doping density as they appear in the single image according to Eq. (1). An additional beneficial aspect of the applications to bricks is the fact that bricks are usually polished prior to wafer cutting. Both the excitation light entering and the luminescence escaping the sample then travel almost perfectly perpendicular to the surface, justifying the one dimensional model used here. Diffusely

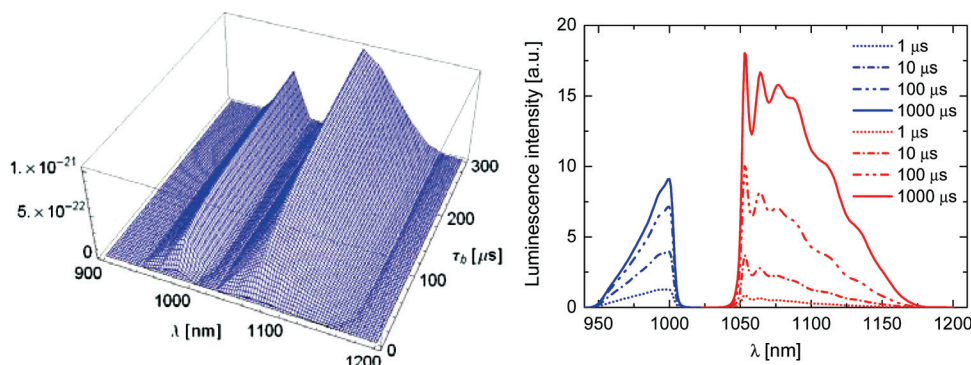


FIG. 3. (Color online) Comparison of the calculated luminescence intensity as a function of wavelength λ and bulk lifetime τ_b for both short (950–1000 nm) and long pass (1050–1180 nm) configuration with a measurement setup using a silicon CCD camera (left). The integral luminescence intensity (right) measured with a long pass filter increases more strongly with increasing bulk lifetime than the signal measured with a short pass filter.

scattering surfaces as they are present at textured or unpolished samples show more complex optical paths, which cannot be described with a one dimensional model anymore.

The photoluminescence intensity ratio could be maximized by simultaneously reducing the short pass filter cutoff and increasing the long pass filter cutoff wavelength, both of which would however result in a reduction in detectable signal and therefore either in reduced signal-to-noise ratio or in longer data acquisition times. The filter combination used in this study was chosen to represent a good compromise between convenient measurement times and sufficient variation in the intensity ratio as to allow reliable conversion of PLIR into bulk lifetime over a wide range of values.

4. Model predictions

The above model leads to a transfer function $PLIR(\tau_b)$, which converts the measured photoluminescence intensity ratio into minority carrier bulk lifetime. Figure 4 shows this function derived for the experimental setup used in this work in linear and double logarithmic scale for both p and n doping at a temperature of 290 K and assuming a $1\Omega\text{cm}$ resistivity in both cases. The dependency is nonlinear, showing the steepest slope for $1 < \tau_b < 1000 \mu\text{s}$, which is beneficial since it allows the most reliable conversion of PLIR into τ_b in the range typically of interest for monocrystalline and multicrystalline silicon used in photovoltaics. The PLIR of n-type silicon is smaller for the same lifetime due to the almost 3 times lower mobility of the holes, which are the minority carriers in n-type material. Since the same PLIR is expected for the same diffusion length for both n- and p-type silicon, the

transfer function is shifted on the bulk lifetime axis by a factor of 3.

It is noted that the transfer function, while being strongly nonlinear does not saturate with increasing bulk lifetime, as it is the case for wafers and solar cells, and allows a reliable conversion of experimental intensity ratio data into bulk lifetime for up to 10 ms bulk lifetime and higher. The equivalent conversion for wafers is limited to about $25 \mu\text{s}$ bulk lifetime due to the strong influence⁸ of two surfaces. Furthermore, once the transfer curve is determined for a specific hardware system it remains valid and is independent to variations in illumination intensity, exposure time, and other experimental parameters, which do not affect the spectral dependency of the measurement. Long term drift in these parameters, e.g., due to a long term deterioration of the laser therefore do not affect the accuracy of this method. And most importantly, the need to measure the background doping, which has a strong influence on the absolute luminescence signal is eliminated.

The above assumption of a $5 \mu\text{m}$ dead layer, however, does affect the detected spectrum due to the additional optical path leading to an increased photon reabsorption of the luminescence light and thus to an increase in the photoluminescence intensity ratio. The quantitative analysis shows that this assumption leads to a 12% decrease in the calculated bulk lifetime.

5. Relative doping density

Single photoluminescence images contain convoluted information about bulk lifetime variation and variations in background doping. Knowledge about one of those

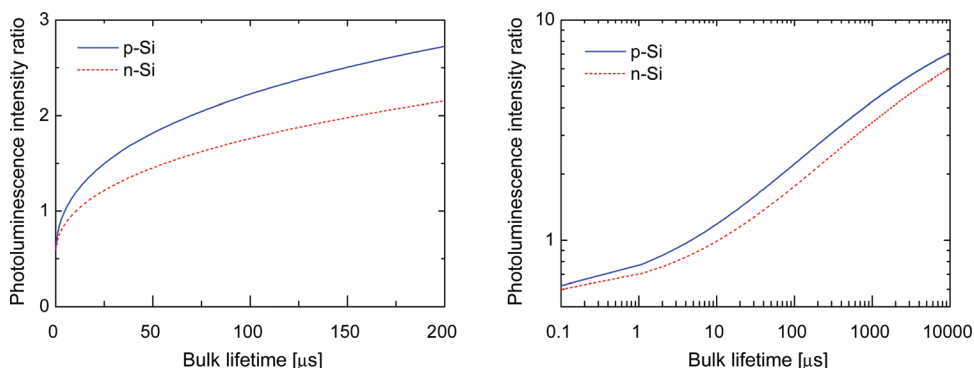


FIG. 4. (Color online) Calculated photoluminescence intensity ratio (PLIR) transfer function as a function of bulk lifetime for the experimental setup used in this study. The PLIR transfer function is shown in both linear (left) and double logarithmic scale (right) revealing a significantly smaller absolute PLIR for n-type than for p-type silicon.

parameters is required in order to extract the second parameter from a single PL image, which requires a separate measurement of the doping concentration in bulk lifetime analysis from a single PL image, as described above. Once the bulk lifetime information is available from the two filter method, as discussed in the previous chapter, the relative doping concentration can also be obtained from each single PL image. In that case the bulk lifetime data from the two filter method combined with the theoretical model described above is used to calculate the doping normalized luminescence intensity. By dividing the measured luminescence intensity PL_{meas} by this normalized luminescence intensity PL_{norm} a relative doping density of activated dopants referring is obtained:

$$N \propto \frac{PL_{\text{meas}}}{PL_{\text{norm}}(\tau_b)} \quad (12)$$

This process can be performed for each of the individual images taken for the two filter method or for a separate image taken with a different filter combination, for example, a conventional PL image taken without additional short or long pass filter. The density of active dopants obtained in this fashion only provides relative doping density variations. After calibration of these relative values, for example by comparison with Eddy current measurements on one specific sample, the approach described above even allows absolute doping density to be obtained. However, similar to the single PL image bulk lifetime method, this approach then relies on the analysis of absolute PL intensities and is therefore susceptible to long term drifts and accurate calibration of each specific experimental system.

III. EXPERIMENTS AND RESULTS

Both methodologies described in this work, i.e., the analysis of a single doping normalized PL image and the analysis of the PLIR, lead to photoluminescence bulk lifetime images. The experimental PL imaging data were obtained using one-sun equivalent homogeneous monochromatic laser excitation in a laboratory PL imaging setup at BT Imaging. Both methods were performed on the polished side faces of multicrystalline, boron doped, block cast silicon bricks with a size of $15.6 \times 15.6 \times 24$ cm. The detection of the luminescence signal was realized by means of a precisely temperature controlled and cooled Si CCD camera with a one megapixel chip providing a spatial resolution of $165 \mu\text{m}$ per pixel. The field of view in that setup is limited to 16.5 cm, requiring two images to be taken on each brick surface. An automated stitching algorithm was used to generate images of the entire brick's surfaces.

A. Single luminescence image

The following measurements and methods were performed in order to obtain a bulk lifetime image by calibration of a single PL image against spatially resolved QSSPC data: A full resolution PL image was measured with 30 s exposure time and an excitation wavelength $\lambda_{\text{exc}} = 808$ nm. No additional filters were used for that measurement beyond

the filters that are required to block the incident laser light from entering the camera. QSSPC bulk lifetime line scans along the growth direction were carried out using a Sinton Instruments BCT210 system. The removal of trapping effects in the QSSPC data was achieved using a customised automated algorithm based on the method described by Macdonald *et al.*¹⁸ Two dimensional Eddy current resistivity maps were measured utilizing a Semilab WT2000-PV system and converted into corresponding maps of the background doping density. The variation of the doping concentration along the growth direction $N(y)$ was obtained from that data by averaging all data points parallel to the growth direction. That curve was re-sampled in intervals matching the PL image resolution and then used to normalize the PL intensity in each pixel.

PL intensities from PL images are generally not measured in absolute units and the theoretical analysis above also predicts only relative variations of the detected photon flux. To account for this a calibration constant, C_{cal} is used in Eq. (2). This calibration constant needs to be determined once and is expected to be valid for different bricks with similar optical surface properties. C_{cal} was determined experimentally by comparison of bulk lifetime data obtained from PL imaging using Eq. (2) with bulk lifetime data from QSSPC. A complication in that calibration procedure arises from the injection dependence of bulk lifetime. A valid comparison would require both PL and QSSPC to be measured at the same injection level. As stated above, PL measures the bulk lifetime at an average injection level of about 10^{13} cm^{-3} . QSSPC data are measured as a function of injection level at each position and can be analyzed in principle at any injection level. However at $n_{\text{av}} < 10^{14} \text{ cm}^{-3}$ the data typically becomes strongly affected by trapping artifacts, even after the above mentioned correction of trapping artifacts.

On one specific center brick investigated in this study the lowest average injection level that could reliably be analyzed was found to be $\Delta n_{\text{av}} = 5 \times 10^{13} \text{ cm}^{-3}$. Further, QSSPC bulk lifetime data from that same brick analyzed at $\Delta n_{\text{av}} = 1 \times 10^{14} \text{ cm}^{-3}$ gave almost identical values, confirming an insignificant injection level dependence in the low injection range. This observation justifies the calibration of the single image photoluminescence data against QSSPC, despite a residual large deviation in average injection level between the QSSPC and the PL measurement by a factor 5.

C_{cal} was determined by conversion of the doping normalized PL image into bulk lifetime according to Eq. (2). C_{cal} was varied to get the best fit between cross section data from bottom to top between QSSPC and PL. An excellent agreement of the cross section data was observed along the entire brick.

Figure 5 illustrates the resulting photoluminescence bulk lifetime image. The left and right hand side correspond to the bottom and top of the ingot, respectively. The bulk lifetime image allows identifying low lifetime regions at the bottom and top of the bricks as well as lower lifetime in areas of high density dislocation networks, which tend to form mostly in the top fraction of the brick. The center of the brick reveals the highest bulk lifetimes in the range of 100–200 μs . Minor surface artifacts showing the polishing pattern

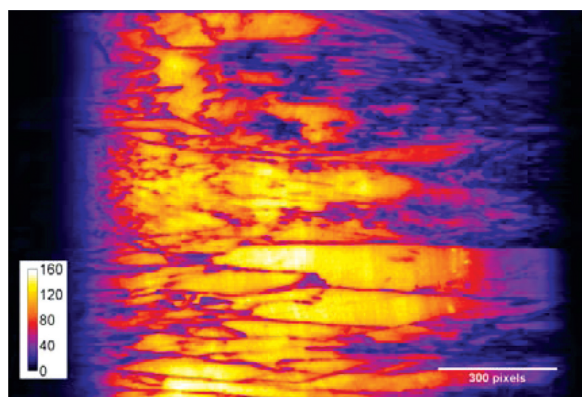


FIG. 5. (Color online) High resolution absolute bulk lifetime image obtained by a single doping normalized photoluminescence image calibrated with QSSPC data. The color scale gives the absolute bulk lifetime in μs . This center brick shows highest lifetimes in the middle of the brick with strong gradients to the bottom and top.

are visible particular within large grains with homogeneous bulk lifetime.

The validity of using the same calibration constant C_{cal} for PL images taken on different bricks was confirmed by measuring a number of production bricks with the same surface polish. A revised transfer function converting QSSPC effective lifetime into bulk lifetime¹⁹ was used here to calibrate the single PL image in Fig. 5. As stated above and in Trupke *et al.*^{9,10} the single PL image method relies on anchoring the PL data to bulk lifetime data from QSSPC, the latter thus being used as reference. Using the revised model resulted in significantly higher bulk lifetime values compared to the bulk lifetime data presented for the same brick in Trupke *et al.*^{9,10} As discussed in our previous study¹⁰ an adjustment of the CCD spectral response was required in the theoretical model in order to match the PL to the QSSPC data. However, the revised QSSPC transfer function results in experimental data, which are more consistent with the PL model using the actual CCD spectral response. The revision of the QSSPC transfer function has thus lead to a dramatically improved consistency with the PLIR data.

While the validity of the single PL image method has been proven to give consistent data for a number of bricks, it has two drawbacks. First, it requires a separate measurement of the absolute doping density across the height of the brick, and second, it relies on analyzing the absolute PL signal and is therefore susceptible to drift in various experimental parameters.

B. Ratio of two luminescence images

An alternative to the single PL imaging method by means of the analysis of a PL intensity ratio is proposed. This is done in analogy to the diffusion length imaging method on finished cells demonstrated by Wuerfel *et al.*² Doping density variations cancel out in the intensity ratio in analogy to the variations in local diode voltages that cancel out in equivalent measurements on solar cells. The intensity ratio method is ideally suited for silicon bricks, since the strong impact of the rear surface are eliminated as the samples are effectively infinitely thick and because the polished

surface allows accurate modeling with a one-dimensional approach.

Two photoluminescence images are measured on the silicon brick side faces using a short and a long pass filter, respectively. The photoluminescence intensity ratio (PLIR) is then calculated for each pixel and finally transferred into a bulk lifetime image by means of theoretically calculated transfer function $PLIR(\tau_b)$.

The incorporation of an additional bandpass filter into the optical setup reduces the detected signal by up to 1 order of magnitude depending on the local bulk lifetime and the type of filter. Longer exposure times are therefore required to achieve the same signal to noise ratio. Shorter exposure times can be achieved in PL imaging via pixel binning on the CCD camera by sacrificing spatial resolution. 3×3 pixel binning was used for the experiments shown here resulting in a spatial resolution of 0.5 mm per pixel and a measurement time for each individual PL image of 30 s. The total measurement time was therefore 60 s for each filter since two images are measured and stitched together in order to cover the entire side face. However, it is noted that the measurements were performed in a comparatively slow laboratory prototype system and optimized optical components will allow a reduction in measurement time of at least a factor 5.

Figure 6 shows the bulk lifetime image obtained by the PL intensity ratio methodology for an edge brick of a silicon ingot. The bottom and the top as well as the edge region show lower lifetimes below 10 μs , whereas bulk lifetimes in the 100–200 μs range were determined in the center region of the brick. It is noted, that this absolute determination of bulk lifetime was performed without any external calibration. A high dynamic range of lifetime and spatial structures are visible in the image as well as large high lifetime grains and low lifetime dislocation cluster. A few small bright spots can be seen in the vicinity of grain boundaries representing an artifact representing a limitation of the one-dimensional model which does not account for lateral minority carrier currents. However, strong variations in bulk lifetime as they are apparent in the vicinity of grain boundaries or dislocation clusters do lead to lateral currents, thus limiting the spatial resolution of the technique. The one-dimensional modeling approach used here breaks down in that case. Quantitatively,

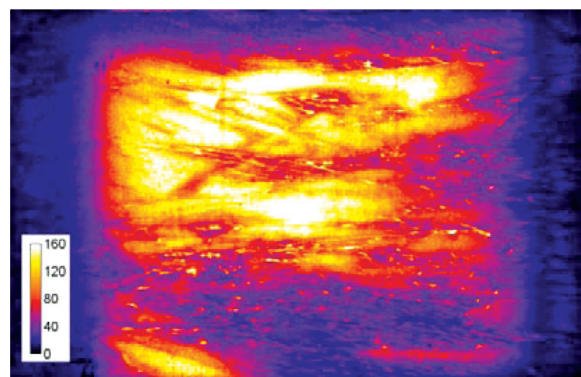


FIG. 6. (Color online) Absolute bulk lifetime image obtained by a photoluminescence intensity ratio from a side face of an edge brick. The color scale gives the absolute bulk lifetime in μs . The vertical stripes are due to surface artifacts caused by an inhomogeneous polish.

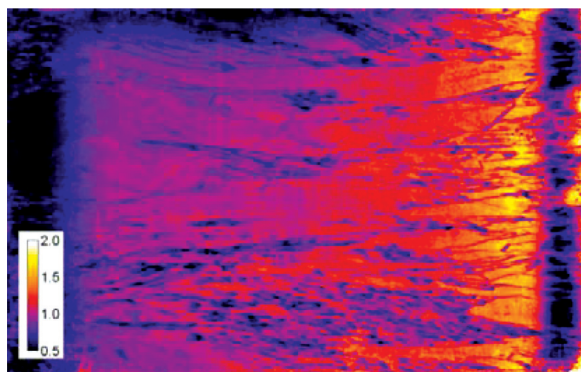


FIG. 7. (Color online) Relative doping density image of the same brick side face as in Fig. 6. The positive gradient of active dopants is visible from bottom to the top of the brick. The illustrated lower doping in the bottom and top region of the brick and in the low lifetime region on the side is caused by an artifact in the PLIR method potentially caused by a defect luminescence signal.

the effect depends on the actual lifetime difference and will be investigated in more detail in further studies which do have to include multidimensional electrical and optical simulation.

Using the theoretical models above the bulk lifetime information obtained from the PLIR method can be used to calculate the expected single photoluminescence image as it would be expected from a brick with constant doping density. The ratio between the measured image and such calculated images gives the variation in background doping. The resulting relative doping density image of the same brick side face is shown in Fig. 7. The expected gradient of active dopants due to segregation during the ingot casting process²⁰ can be seen clearly with increasing concentration of active boron dopants toward the top part of the brick. Grain boundaries appear with lower relative doping as well as the top and the bottom of the brick.

IV. DISCUSSION

A. Validity of bulk lifetime and doping imaging data

The two bulk lifetime imaging techniques presented in this work are based on quite different methodologies. The

validity of the obtained data is therefore further discussed by comparison of measurement results and by fitting to theoretical models.

Figure 8 shows the direct comparison of two photoluminescence bulk lifetime images of the same brick side face and corresponding line scan data in growth direction. The images were obtained from the two methods described above, i.e., by calibration of a doping normalized image (left) and from the PLIR method (right). The qualitative agreement of both images is excellent and both methodologies also show good quantitative consistency in the central, high lifetime part of the brick. The line scan shows excellent quantitative agreement of both methodologies in the central area (0.2–0.85 fraction) of the brick. However, both PLIR image and PLIR line scan data report significantly higher values of lifetime in the low lifetime regions especially in the top and bottom regions, but also at a dislocation site of the brick as shown by arrows in Fig. 8. An edge brick, as shown in Fig. 6, additionally shows a low lifetime side at the surface which was in contact with the crucible during crystallisation and also shows higher than expected bulk lifetime from PLIR data in this area.

It is known from other studies^{21–23} that the bottom and the top of the ingot as well as the edge zones contain much higher impurity concentrations (e.g., transition metals) than the center part of the ingot. This is the result of solid-state diffusion of impurities from the crucible after crystallisation has occurred or of back diffusion from the top the ingot during cooldown. An additional defect luminescence signal with contributions in the long wavelength range (1100–1300 nm), would explain the observed overestimation of the apparent bulk lifetime and is currently thought to be the cause for the artifacts observed in the PLIR method in the lowest lifetime regions. Spectral luminescence measurements from those low lifetime regions will shed more light on this issue.

Cross section data of the relative doping density from Fig. 7 are shown in Fig. 9 providing another strong indication for corrupting defect luminescence in lowest lifetime regions of the brick. The cross section of active boron dopants can be fitted nicely to the Scheil equation²⁰ which was expanded by Burton *et al.*²⁴ who introduced the important concept of the effective segregation coefficient k_{eff} . The

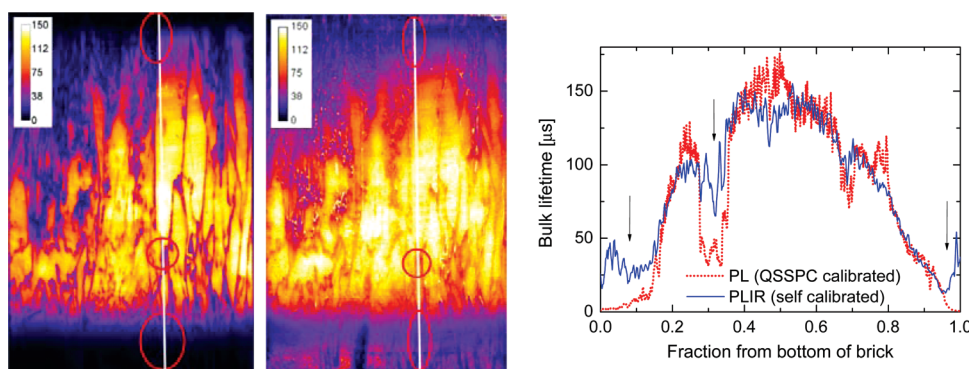


FIG. 8. (Color online) Bulk lifetime from a single PL image calibrated with QSSPC (left) in direct comparison with the PLIR image (middle) of the same brick side face. Both images are shown on the same relative color scale revealing good qualitative and quantitative agreement in the center part of the brick. The indicated line scan confirms good quantitative agreement in high lifetime regions in the central part of the brick (right). Artificially high lifetimes are reported by the PLIR method in areas of low lifetime especially at the top and bottom of the brick as indicated.

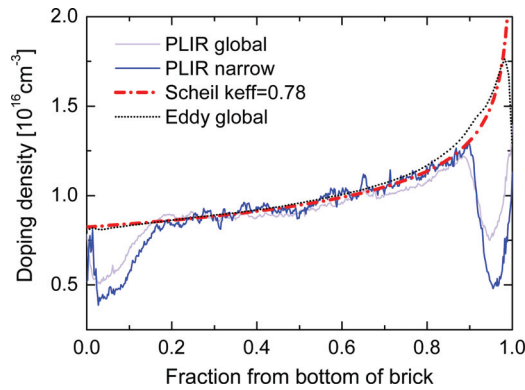


FIG. 9. (Color online) Doping density profile obtained from photoluminescence intensity ratio throughout the brick in comparison with Eddy current data and the Scheil equation. The photoluminescence data matches well to both the Eddy current data and the calculations from the Scheil equation in the center of the brick (fraction 0.2–0.85), but it does not contain correct doping density information in the bottom and top region of the brick. A particular good match of the luminescence data is found in a narrow quasi-monocrystalline part of the brick (labeled PLIR narrow).

latter correlates the effect of convection and nonperfect mixing of dopants on solute segregation along the axis of the crystal in terms of average solute concentration grown into the crystal and the concentration of the bulk melt as:

$$k_{eff} = \frac{\langle C_s \rangle}{\langle \langle C \rangle \rangle} \quad (13)$$

where $\langle \langle C \rangle \rangle$ is the volume averaged concentration in the melt and $\langle C_s \rangle$ is the average concentration in the crystal at the melt/crystal interface.²⁵ Using this convection corrected description of the segregation coefficient the Scheil equation can be written correspondingly as

$$C_s = k_{eff} C_0 (1 - f_s)^{k_{eff}-1} \quad (14)$$

where C_0 is the initial composition in the liquid and f_s the solidified fraction. Figure 9 shows that the Scheil equation fits the luminescence intensity ratio data well in the range of 0.2–0.85 fraction from the bottom of the brick, whereas it strongly deviates from the theoretical distribution in the bottom and top of the brick. The analysis of doping density proposed in this work is based on the bulk lifetime data obtained by utilizing the PLIR method. In the lowest lifetime regions, where the PLIR method is affected by the above mentioned artifacts, the calculation of doping density will therefore fail. However, it shows to be an excellent measure in pure, large crystal grains (see PLIR narrow in Fig. 9).

The best theoretical fit to the measurement data was achieved by choosing $k_{eff} = 0.78$ which is very close to the data reported for boron in Czochralski grown silicon.^{26,27} The fit is also in good agreement with the Eddy current data taken on the same brick side face by means of a Sinton Instruments BCT210.

B. Limitation on spatial resolution

The photoluminescence intensity ratio methodology presented here is based on a one-dimensional model and is thus

strictly valid only for monocrystalline ingots with small lateral changes in bulk lifetime. However, it is also valid for bulk variations within large grains in multicrystalline bricks, occurring for example due to variations in the concentration of atomic impurities such as iron. Some limitations on the accuracy of the method presented in this work are expected for smaller scale spatial features with feature sizes on the order of the sense depth of the PL signal, which is in the order of 1–2 mm. Small grains and dislocation networks are examples for such features. The one-dimensional model breaks down in that case, since the carrier density profile is no longer predominantly governed by the diffusion of excess carriers into the depth of the brick but also by lateral diffusion toward nearby lower lifetime features. An analysis of the impact of such small scale lateral variations in bulk lifetime on the PL intensity ratio method and resulting limitations using two- and three-dimensional modeling is currently in progress but beyond the scope of this paper. Here we need to be aware that some features, for instance the bright spots in the area of high dislocation density and in the vicinity of grain boundaries (e.g., see Figure 6) are likely caused by such effects.

C. Calibration and measurement uncertainties

The calibration of the single PL image methodology is achieved by separate QSSPC line scans in order to obtain the calibration constant C_{cal} of Eq. (2). Line scans are taken in growth direction of the brick with each of about 45 spots measured, locally averaging the bulk lifetime. The calibration of the QSSPC technique itself has recently been investigated theoretically in more depth resulting in a new calibration function which transfers the measured effective lifetime into bulk lifetime.¹⁹ The new analysis found the sense depth of the conductance measurement sensor to be limited to 0.25 cm. This led to a substantial underestimation of the apparent bulk lifetime in former studies.¹¹

The photoluminescence intensity ratio based bulk lifetime imaging allows a conversion of the experimental data into bulk lifetime by pure modeling of the experiment without the need of a second measurement technique. The intensity ratio at a given temperature is purely dependent on all wavelength dependent parameters like filter transmission and camera objective optical characteristics, detector CCD sensitivity, and the excitation wavelength. All of these parameters can be measured quite accurately and are not subject to change or drift once the system is assembled. Other parameters like the laser intensity and homogeneity have to be kept constant between the two PL measurements, but then cancel out in the PLIR. This leads to a lower sensitivity to long-term shifts in experimental parameters like the illumination and removes the need for an absolute calibration of the setup on a regular basis. Other influences on the absolute intensity, such as variations in the thickness of surface damage layers also have a dramatically reduced impact on the bulk lifetime information from the PLIR, compared to the analysis of a single PL image.

Specific parameter uncertainties and their impact on the intensity ratio transfer function are now discussed in order to

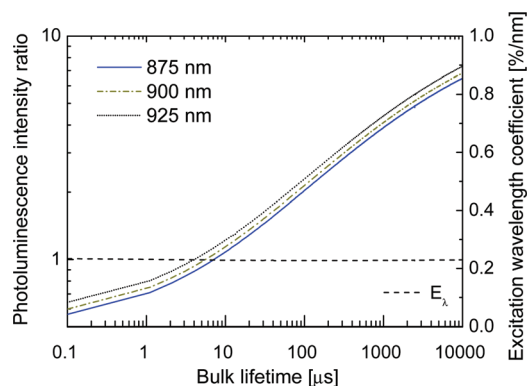


FIG. 10. (Color online) The intensity ratio transfer function calculated for three different excitation wavelengths on double logarithmic scale for p-type silicon. The ratio increases with increasing laser excitation wavelength. The corresponding coefficient is calculated to be constant with bulk lifetime at 0.23% per nm.

estimate a measurement uncertainty regarding bulk lifetime. Since the analysis is somewhat dependent on the type and concentration of the sample doping, this discussion focuses on 1 Ω cm p-type silicon.

The first parameter potentially leading to an uncertainty is the excitation wavelength λ_{ex} . Figure 10 shows the calculated intensity ratio function for different excitation wavelength reporting an increasing intensity ratio with longer excitation wavelength. The ratio is found to scale almost linearly with excitation wavelength across the entire bulk lifetime range, the corresponding coefficient is determined to be 0.23% per nm for the experimental setup used here. An uncertainty in the maximum excitation wavelength of $\Delta\lambda_{ex} \leq \pm 1$ nm would therefore assure an uncertainty in bulk lifetime of well below $\pm 1\%$ relative for all bulk lifetimes.

High power laser diodes, commonly used for PL imaging typically have a Gaussian spectral distribution with a full width half maximum of about 6 nm. The spectral variation within the illumination is therefore small justifying the monochromatic approach used in our model. Unlike other light sources such as light emitting diodes or flash lamps that do show a broad light spectrum which cannot be neglected in calculation of the carrier generation.

Secondly, the sample temperature influences the minority carrier mobility $\mu(N_A, T)$ and the absorption coefficient $\alpha(\lambda, T)$, resulting in a temperature dependent excess carrier profile and reabsorption as discussed above. The temperature dependence of the absorption coefficient also translates into a temperature variation in the radiative recombination coefficient¹⁵ and in changes in the spectral distribution of the emitted photons according to the Generalized Planck law.¹⁶ The sample temperature impact on the transfer function was calculated and is shown in Fig. 11 reporting a negative temperature coefficient of $-0.5\%/K$ at 100 μ s and $-0.7\%/K$ at 1000 μ s. Assuming a reasonable accurate temperature determination prior to measurement with an accuracy of $\pm 1K$, the temperature dependence of the sample would result into an uncertainty of $\pm 0.5\%$ ($\pm 0.7\%$) in the intensity ratio transfer function which transfers into $\pm 1.8\%$ ($\pm 2.8\%$) uncertainty in bulk lifetime at 100 μ s and 1000 μ s, respectively. Thus, an accurate sample temperature measurement can strongly

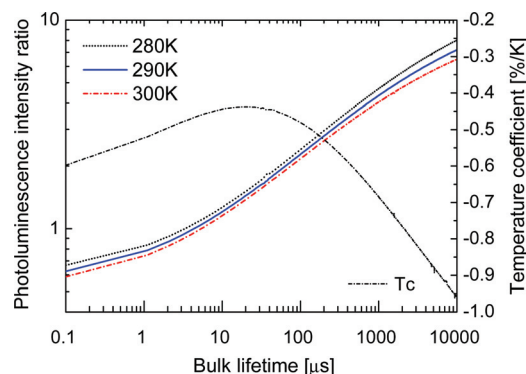


FIG. 11. (Color online) Intensity ratio transfer function calculated for three different sample temperatures on double logarithmic scale for p-type silicon. The ratio reduces with increasing temperature resulting in a negative temperature coefficient. The temperature induced change in the intensity ratio can be quantified to be in the range of -0.4 to -1% per Kelvin finding its minimum at around 20 μ s.

reduce the impact of temperature on the bulk lifetime. A similar sensitivity to temperature changes is also present in the silicon CCD detector array. However, in the scientific CCD cameras commonly used for PL imaging the array is precisely temperature controlled and uncertainties can therefore be neglected.

Additional uncertainties are originated in the filter characteristics and the spectral sensitivity of the detection CCD mainly due to their strong spectral dependency. The filter characteristic can be measured accurately with a near infrared (NIR) photo spectrometer achieving a spectral accuracy of below ± 0.1 nm and a transmission accuracy equivalent to a relative error of below $\pm 1\%$ relative. The spectral uncertainty of the cut-off wavelength in both short and long pass filter result in relative uncertainties of $\pm 0.6\%$ for both 100 and 1000 μ s bulk lifetime on the intensity ratio transfer function. It is noted that a lower spectral accuracy would cause a strong increase in measurement uncertainty, especially in case of the long pass filter, the spectral cutoff being located in a spectral range where the luminescence spectrum has a particularly steep slope.

The spectral sensitivity of the silicon CCD and the camera objective are difficult to measure precisely, especially in the long wavelength range above 1050 nm near the silicon absorption edge resulting in quantum efficiencies below 5%. However, the spectral sensitivity of the CCD has a strong impact on the intensity ratio due to a high gradient in quantum efficiency in the spectral range of interest for crystalline silicon. Addressing this, the model presented here incorporates a measured CCD quantum efficiency in the range 800–1050 nm and then models the respective values in the range 1050–1300 nm by calculating the absorption of the silicon CCD represented by a planar silicon slab. The thickness of this slab is then chosen to match the measured quantum efficiency at 1050 nm and thus allows estimating the CCD quantum efficiency in the extended wavelength range in a continuous way.

However, since a simple slab is a strong idealization of a CCD chip the experimental parameter uncertainty of this study can be estimated to be up to $\pm 5\%$ which leads to a

TABLE I. Estimated parameter uncertainties and calculated resulting uncertainties on the intensity ratio transfer function PLIR and on the bulk lifetime τ_b itself.^a

	λ_{ex} (± 1 nm)	Sample T (± 1 K)	Filter cut off (± 0.1 nm)	Filter transmission ($\pm 1\%$ rel.)	CCD + objective ($\pm 2\%$ rel.)	Σ PLIR	$\Sigma\tau_b$
100 μ s	± 0.2	± 0.5	± 0.6	± 0.8	± 1.7	± 3.8	± 13.5
1000 μ s	± 0.2	± 0.7	± 0.6	± 0.7	± 1.4	± 3.6	± 14.9

^aTable values are given in per cent for p-type 1 Ω cm silicon and were calculated for the experimental setup used in this study. The estimated uncertainty increases with increasing bulk lifetime since the slope of the PLIR transfer function reduces slightly above about 100 μ s.

systematic parameter uncertainty in absolute bulk lifetime of up to $\pm 16\%$. Careful characterization of the CCD quantum efficiency would reduce the uncertainty on the spectral sensitivity to $\pm 2\%$ leading to a relative uncertainty of $\pm 1.7\%$ in the intensity ratio at 100 μ s lifetime ($\pm 1.4\%$ at 1000 μ s) or 6.1% in bulk lifetime at 100 μ s (5.6% at 1000 μ s), respectively. The good absolute agreement of both PLIR and QSSPC calibrated images shown in Fig. 8 motivates the choice of this reduced $\pm 2\%$ uncertainty on the CCD sensitivity for the following calculation of the total uncertainty assuming a setup characterization following best practice.

Table I lists the discussed parameters uncertainties and their calculated impact on the uncertainty of the intensity ratio value (PLIR). The estimated total uncertainty on the prediction of the bulk lifetime is determined to be $\pm 13.5\%$ at 100 μ s (14.9% at 1000 μ s) for the experimental setup used in this work assuming listed parameter uncertainties.

The above photoluminescence intensity ratio uncertainties are mainly caused by systematic errors, which can be reduced by careful characterization of the hardware and careful measurement of, e.g., the sample temperature. Importantly, the statistical errors are very small which represent a major advantage of the intensity ratio technique and other purely photoluminescence imaging based techniques as they are very reproducible.

The systematic error on the absolute bulk lifetime can potentially be reduced by using a different CCD camera type with higher and less variable quantum efficiency in the range of the photoluminescence emission.

V. CONCLUSIONS

The quantitative determination of bulk lifetime images on the side faces of silicon bricks by using photoluminescence imaging has been discussed. Two different methodologies have been presented theoretically and experimentally. The PLIR based technique is advantageous, because it eliminates both the need for a separate resistivity scan and for a separate calibration measurement against QSSPC. It was shown, that careful characterization of the spectral sensitivity of the measurement setup can reduce the relative systematic error in bulk lifetime to below $\pm 15\%$. Once the system is calibrated, the PLIR method leads to stable and reproducible measurements well suited for quality control in industry without being sensitive to long term shifts in laser intensity or homogeneity.

Furthermore, a qualitative imaging of the doping density throughout the brick was demonstrated and discussed. The

intensity ratio based data could be fitted to the theoretical Scheil equation in the center section of the brick providing a fast and reliable method to image the doping profile after crystallisation.

Further work will investigate the artifacts that are observed in bulk lifetime images obtained from the PLIR (and as a result in relative doping images) within high impurity parts of the ingot (bottom, top, edge). These artifacts are currently thought to be caused by defect luminescence. Further studies also have to investigate the PLIR model in two or three dimensions in order to expand the valid bulk lifetime prediction into high dislocation clusters and small grain structures.

The presented methods provide new methodologies to gain a contactless, nondestructive, high resolution bulk lifetime, and doping images. The bulk lifetime analysis of cast silicon bricks after directional solidification can potentially be applied for wafer sorting prior to wafer cutting and for optimization of the crystallization process.

ACKNOWLEDGMENTS

Bernhard Mitchell gratefully acknowledges financial support by the German Academic Exchange Service (DAAD). The work was supported by the Australian Research Council through the Photovoltaics Centre of Excellence.

- ¹T. Trupke, R. A. Bardos, M. C. Schubert, and W. Warta, *Appl. Phys. Lett.* **89**, (2006).
- ²P. Wuerfel, T. Trupke, T. Puzzer, E. Schäffer, and W. Warta, *J. Appl. Phys.* **101**, 123110 (2007).
- ³T. Trupke, *J. Appl. Phys.* **100**, 063531 (2006).
- ⁴J. A. Giesecke, M. Kasemann, M. C. Schubert, P. Wuerfel, and W. Warta, *Prog. Photovoltaics* **18**, 10 (2010).
- ⁵J. A. Giesecke, M. Kasemann, M. C. Schubert, B. Michl, M. The, W. Warta, and P. Wuerfel, in *Proceeding of the 23rd European Photovoltaic Conference* (Valencia, Spain, 2008).
- ⁶J. A. Giesecke, M. Kasemann, and W. Warta, *J. Appl. Phys.* **106**, 014907 (2009).
- ⁷R. A. Sinton and A. Cuevas, *Appl. Phys. Lett.* **69**, 2510 (1996).
- ⁸K. Bothe, R. Krain, R. Falster, and R. Sinton, *Prog. Photovoltaics* **18**, 204 (2010).
- ⁹T. Trupke, J. Nyhus, R. A. Sinton, and J. W. Weber, in *Proceedings of the 24th European Photovoltaic Conference* (Hamburg, 2009).
- ¹⁰T. Trupke, B. Mitchell, J. W. Weber, and J. Nyhus, in *Proceedings of the 25th European Photovoltaic Conference* (Valencia, Spain, 2010).
- ¹¹S. Bowden and A. Sinton, *J. Appl. Phys.* **102**, 124501 (2007).
- ¹²M. A. Green, *Sol. Energy Mater. Sol. Cells* **92**, 1305 (2008).
- ¹³G. Masetti, M. Severi, and S. Solmi, *IEEE Trans. Electron Devices* **30**, 764 (1983).
- ¹⁴S. Reggiani, M. Valdinoci, L. Colalongo, M. Rudan, and G. Baccarani, *VLSI Design* **10**, 467 (2000).

- ¹⁵T. Trupke, M. A. Green, P. Würfel, P. P. Altermatt, A. Wang, J. Zhao, and R. Corkish, *J. Appl. Phys.* **94**, 4930 (2003).
- ¹⁶P. Wuerfel, *J. Phys. C* **15**, 3967 (1982).
- ¹⁷H. R. Philipp and E. A. Taft, *Phys. Rev.* **120**, 37 (1960).
- ¹⁸D. Macdonald, R. A. Sinton, and A. Cuevas, *J. Appl. Phys.* **89**, 2772 (2001).
- ¹⁹J. S. Swirhun, R. A. Sinton, M. K. Forsyth, and T. Mankad, *Prog. Photo-voltaics* (published online) (2010).
- ²⁰E. Scheil, *Z. Metallkd.* **34**, 70 (1942).
- ²¹R. Kvande, L. J. Geerligs, G. Coletti, L. Arnberg, M. Di Sabatino, E. J. Øvrelid, and C. C. Swanson, *J. Appl. Phys.* **104**, 064905 (2008).
- ²²D. Macdonald, A. Cuevas, A. Kinomura, Y. Nakano, and L. J. Geerligs, *J. Appl. Phys.* **97**, 033523 (2005).
- ²³M. Rinio, C. Ballif, T. Buonassisi, and D. Borchert, in *Proceedings of the 19th European Photovoltaic Solar Energy Conference* (Paris, 2004).
- ²⁴J. A. Burton, R. C. Prim, and W. P. Slichter, *J. Chem. Phys.* **21**, 1987 (1953).
- ²⁵R. A. Brown and D. H. Kim, *J. Cryst. Growth* **109**, 50 (1991).
- ²⁶P. S. Ravishankar, L. P. Hunt, and R. W. Francis, *J. Electrochem. Soc.* **131**, 872 (1984).
- ²⁷H. Kodaera, *Japanese J. Appl. Phys.* **2**, (1963).